Resonant ultrasound elastic characterization of steel wire arc additive manufacturing samples

Le Bourdais, Florian; Mahmoudiniya, Mahdi; Gardahaut, Audrey; Kestens, Leo A.I.

DOI
10.1016/j.matchar.2024.114603

Publication date
2025

Document Version
Final published version

Published in
Materials Characterization

Citation (APA)
Le Bourdais, F., Mahmoudiniya, M., Gardahaut, A., & Kestens, L. A. I. (2025). Resonant ultrasound elastic characterization of steel wire arc additive manufacturing samples. *Materials Characterization*, *220*, Article 114603. https://doi.org/10.1016/j.matchar.2024.114603

Materials Characterization 220 (2025) 114603

Contents lists available at ScienceDirect

Materials Characterization

journal homepage: www.elsevier.com/locate/matchar

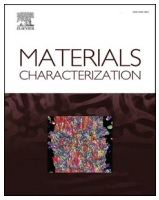

Resonant ultrasound elastic characterization of steel wire arc additive manufacturing samples

Florian Le Bourdais [a,*], Mahdi Mahmoudiniya [b], Audrey Gardahaut [a], Leo A.I. Kestens [b,c]

[a] Université Paris-Saclay, CEA, F-91120 Palaiseau, France
[b] Ghent University, Metal Science and Technology Group, Technologiepark 46, 9052 Gent, Belgium
[c] Delft University of Technology, Materials Science and Engineering, Mekelweg 2, 2628 CD Delft, the Netherlands

ARTICLE INFO

Keywords:
Additive manufacturing
Resonant ultrasound spectroscopy
electron backscattered diffraction
X-ray diffraction
Texture analyis
Elastic modelling

ABSTRACT

Wire Arc Additive Manufacturing (WAAM) is a metal Additive Manufacturing (AM) technique that can produce fully dense metallic structures with virtually no porosity and at high productivity, compared to other currently available AM techniques such as Laser Powder Bed Fusion (L-PBF). As development of the technique is still ongoing, monitoring or post-fabrication inspection methods are under active investigation. In this work, we apply Resonant Ultrasound Spectroscopy (RUS) to samples fabricated from two different wires (construction steel and austenitic stainless steel) and quantitatively characterize isotropic and anisotropic elastic behaviour of the obtained dense parts. We find that an isotropic elastic model fits the construction steel samples well. For the 316 L polycrystal however, the isotropic elastic model is unsatisfactory, and an effective orthotropic elastic model is found to fit the resonance data. EBSD and XRD measurements are used to confirm and explain this difference in elastic behaviour between steel grades by the presence of a strong texture in the 316 L samples. Additionally, the texture data measured by EBSD are used to infer single crystal constants from the polycrystal resonance data using the Hill averaging scheme for one of the 316 L samples. We end by discussing the differences between the two elastic models used in the study (orthotropic and texture based) as well as the link between the measured resonances and microstructural descriptions of the samples.

1. Introduction

Wire Arc Additive Manufacturing (WAAM) is a metal Additive Manufacturing (AM) technique that can produce fully dense metallic structures with virtually no porosity and at high productivity, compared to other currently available AM techniques such as Laser Powder Bed Fusion (L-PBF). As development of the technique is still ongoing, monitoring or post-fabrication inspection methods are being actively developed [1]. Resonant Ultrasound Spectroscopy (RUS) [2,3] is a non-destructive characterization technique that enables the characterization of elastic material properties based on the propagation of elastic waves in the bulk of the object under examination. It is a good candidate for post-fabrication inspection of samples, such as manufactured by WAAM, as it is sensitive to a combination of density, elastic and geometric factors and can be used to detect defects [4].

RUS has already been widely applied to AM samples and parts. Some authors have used RUS as a method for defect detection and classification of samples. McGuigan et al. [5] fabricated lattice arches with missing struts and compared experimental resonance frequencies to simulated ones using finite element models. Obaton et al. [6] also used RUS to sort complex as-built specimens into different classes depending on process parameters and geometry parameters, showing the high sensitivity of the method to the input parameters. Bozek et al. [7] used nonlinear RUS to characterize 316 L-PBF samples after different heat treatments, showing qualitative links between the evolution of the microstructure and the RUS measurement. Manogharan et al. [8] investigated the applicability of nonlinear RUS to configurations that resemble *in situ* monitoring in AM machines. Le Bourdais et al. [9] used RUS to characterize L-PBF aluminium samples and have shown numerous correlations between porosity and elastic resonance measurements.

Other authors have focused on applying the RUS methodology to quantitative analysis of texture and its evolution. Rossin et al. [10] investigated effects such as recrystallization after heat treatment and grain structure evolution, documenting a reduction in the dominant ⟨100⟩ texture with RUS and EBSD measurements. Rossin et al. [11]

* Corresponding author.
E-mail address: florian.lebourdais@cea.fr (F. Le Bourdais).

https://doi.org/10.1016/j.matchar.2024.114603
Received 11 October 2024; Received in revised form 29 November 2024; Accepted 2 December 2024
Available online 12 December 2024

Table 1
Chemical compositions for S620 and 316 L wires (wt%), taken from constructor datasheets.

Wire type	C (%)	Si (%)	Mn (%)	P (%)	S (%)	Cr (%)	Ni (%)	Mo (%)	Cu (%)	V (%)	N (%)
S620	0.10	0.73	1.60	0.009	0.005	0.56	0.54	0.27	0.03	0.01	–
316 L	0.015	0.45	1.6	–	–	18.5	12.0	2.6	–	–	0.04

Table 2
Deposition parameters for samples in this study.

Wire type	Size of wire (mm)	Current (A)	Voltage (V)	Type of current	Contact-tip to work-piece distance (CTWD) (mm)	Travel speed (mm/min)	Gas flow (l/min)
S620	1.2	220	18.2	DC	15	650	16
316 L	1.2	195	13.5	DC	17	450	15

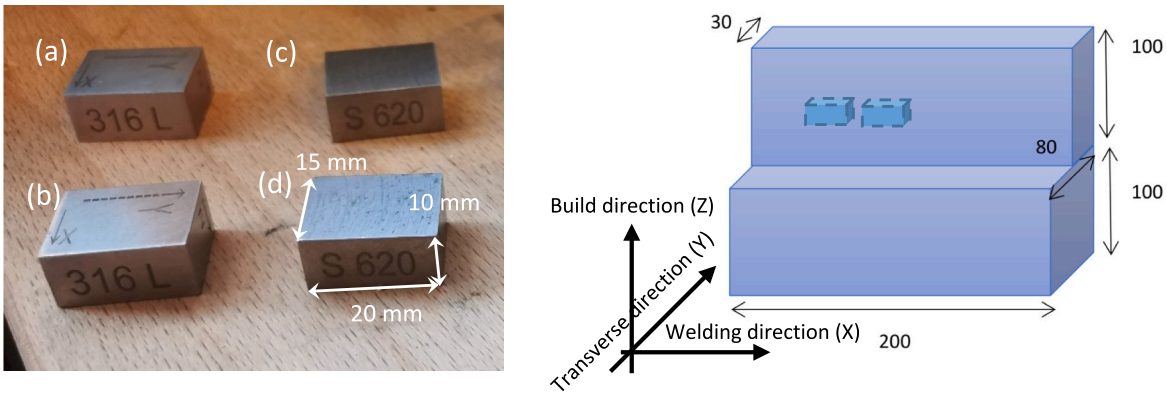

Fig. 1. (left) Metallic samples analysed in this study: austenitic 316 L samples (a) and (b), S620 samples (c) and (d). (right) Schematic depiction of S620 samples original location within massive block with block reference frame (identical to sample reference frame).

performed RUS inversion using a tensorial texture representation of the ODF-coefficients with known single crystal constants and obtained good agreement with EBSD data. Rossin et al. [12] investigated how to characterize single crystal coefficients from polycrystalline alloys using RUS and EBSD, which helps avoiding the expense of growing single crystals or synchrotron experiments.[1]

This short literature review suggests that RUS is well suited for elastic analysis of AM samples and in particular for indirectly obtaining information about texture through the determination of elastic constants. In this work, we therefore propose to apply it to samples produced by the WAAM process with the aim to assess whether we can link the resonant spectra to microstructural characteristics of the samples. Our paper is organized as follows: we first describe the fabrication of the four samples under study and the analysis methods (RUS, EBSD, XRD) in section 2. We describe, in particular, the three inverse models used in our RUS analysis: an elastic isotropic model, an effectively orthotropic model, and a EBSD-texture model based on the Hill averaging scheme. We then present the results from RUS, EBSD and XRD in section 3. Finally, we discuss the differences between the RUS inverse models and how they relate effective part-scale properties to microstructure in section 4.

2. Sample description and analysis methods

The following section describes the samples analysed in this study, as well as the analysis methods used.

2.1. Sample fabrication

Our study involved two types of steel: stainless steel 316 L and structural steel S620. Table 1 presents the chemical composition of the wires used to print the coupons. The original blocks were printed at Naval Group using a GMAW (Gas Metal Arc Welding) - CMT (cold metal transfer) machine. Table 2 shows the deposition parameters. Two samples for each steel were extracted from the printed block using a cutting machine. Fig. 1 displays the dimensions of the printed parts, the dimensions of the extracted samples (all 10 mm × 15 mm × 20 mm) and the location of the sample extraction.

2.2. EBSD

We measured the crystallographic texture by electron backscattered diffraction (EBSD) technique. To prepare for EBSD measurements, samples were polished using standard mechanical polishing steps, followed by polishing with colloidal silica suspension. The EBSD measurements were conducted using a field emission scanning electron microscope (FEI-Quanta 450) set to an accelerating voltage of 20 kV, a working distance of 18 mm, and a tilt angle of 70°. The measurements were taken with a step size of 3 μm. The post-processing of EBSD data was carried out using OIM software V 8. The ODFs, derived from the EBSD maps, were obtained by superimposing Gaussian functions with a scatter of 5° on each discrete pixel of the scan. The ODFs, derived from the EBSD maps, were obtained by superimposing Gaussian functions with a scatter of 5° on each discrete orientation corresponding to the individual pixels of the scan. The texture was calculated using the Generalized Spherical Harmonic Expansion (GSHE) method with a maximum rank of 16.

[1] Most of this work is summarized in Jeff Rossin's thesis [13] and has been published as open-source codes (CmdStan RUS [14] and Texture-Rus [15]).

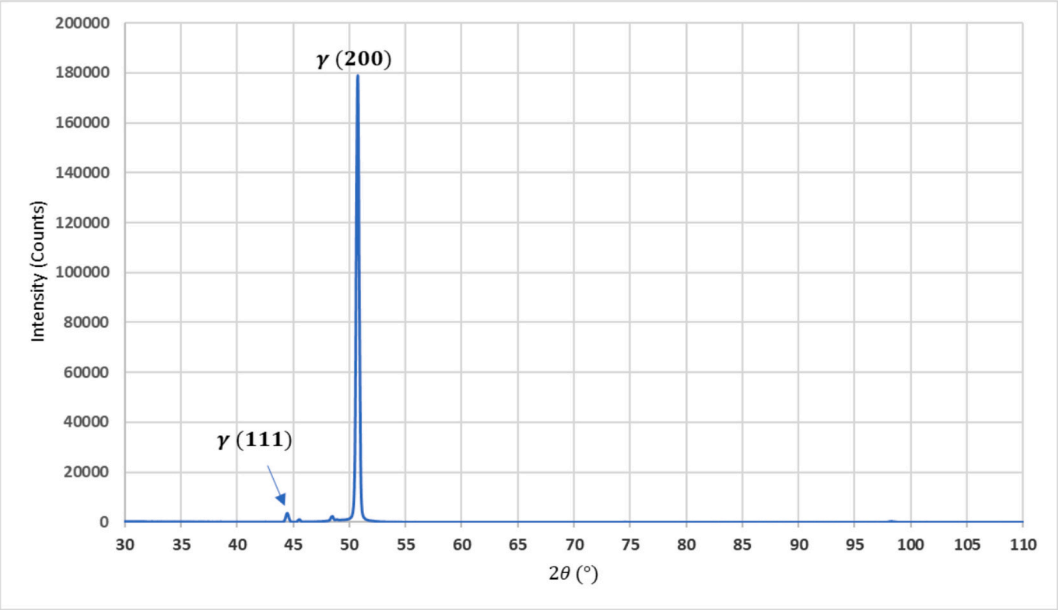

Fig. 2. XRD pattern of one of the WAAM processed 316 L stainless steel, showing intensity of selected austenite peaks.

2.3. XRD

To carry out phase analysis, the conventional X-ray diffraction (XRD) method was employed using a Bruker D8-Advanced diffractometer. A copper Kα tube was used as the target, and the scan step size was 0.02 degrees over the 2θ range from 30 to 110°. The XRD diffractometer was operated using a current of 40 mA and a voltage of 40 kV. The XRD patterns were then analysed using Xpert high-score software.

2.4. Resonant ultrasound spectroscopy

2.4.1. Fundamentals and experimental device

To perform resonant ultrasound spectroscopy measurements, an experimental apparatus already described in [9] was used. The system uses a network vector analyser and piezoelectric sensors to probe the sample with sinusoidal ultrasonic waves at different frequencies to produce a resonance spectrum. We measured each sample several times. As is habitual for resonance measurements, the sample was remounted each time, to avoid missing peaks [2]. The measurement setup is shown in Fig. 3.

To accurately record geometry and density used in resonant ultrasound inversion, samples were weighed with a precision of 0.01 g and the dimensions measured using a digital calliper with a precision of 0.1 mm.

The obtained spectra were then processed, and peaks were extracted. This was done by manually defining peak locations and fitting a Lorentzian model to the recorded magnitude data using the *lmfit* software library [16]. To obtain elastic constants that fit the extracted peaks, the RUS inverse problem was solved using an in-house code. The inverse problem was solved using the Bayesian RUS methodology described in [14]. This involves two main components: the forward model and defining a posterior probability data model.

The forward model used in this work is based on the XYZ algorithm [17] that involves solving the elastic free vibration equations of motion using a high-order polynomial Rayleigh-Ritz approximation. In practice, the method inputs are density ρ, elastic constants c_{ij} and cube geometry defined by side lengths l_1, l_2, l_3. The method assembles a mass matrix $\boldsymbol{M}$ and a stiffness matrix $\boldsymbol{K}$ and yields eigenvalues ω_i^2 and eigenvectors $\boldsymbol{a}$ that satisfy $\omega_i^2 \boldsymbol{M}\boldsymbol{a}_i = \boldsymbol{K}\boldsymbol{a}_i$(with $i = 1, \ldots, 3$).

The posterior probability used in the inverse problem is:

$$P(\theta|M) \propto P(M|\theta)P(\theta), \quad (1)$$

where $P(\theta)$ is the *a priori* probability of the unknown parameter set θ

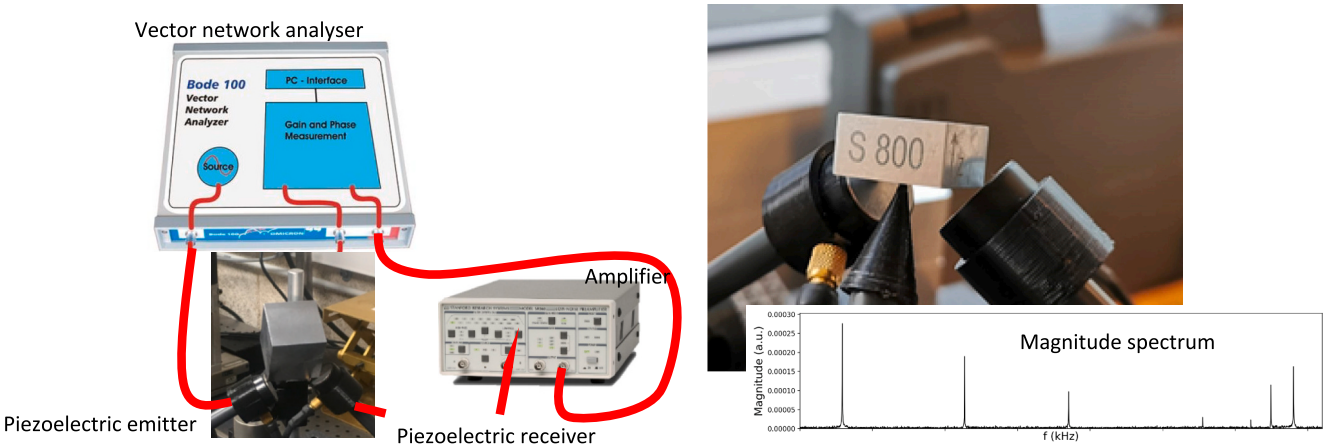

Fig. 3. Experimental setup used for resonance frequency measurement and example magnitude spectrum.

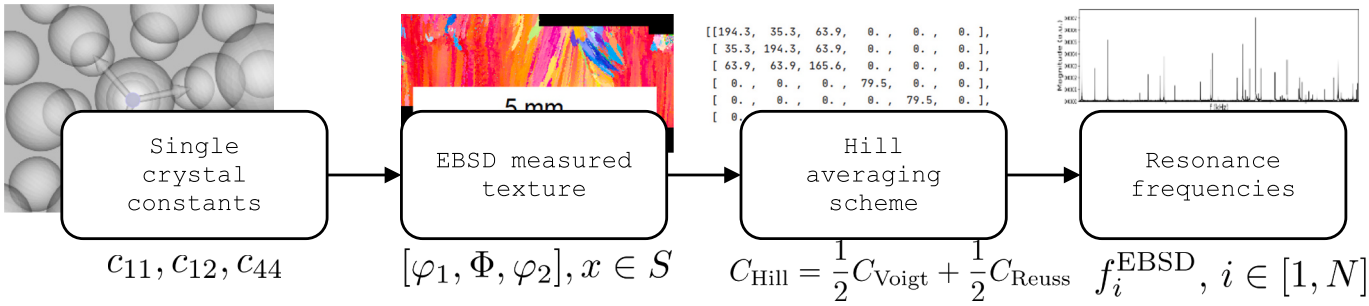

Fig. 4. Schematic description of the model based on measured texture and single crystal elastic constants.

(in our study, this set is the relevant elastic constants defining the c_{ij}) and $P(M|\theta)$ is the likelihood of the measured frequencies given the frequencies computed by the parameter set θ. The *a priori* probability incorporates prior information on the elastic constants. The likelihood is defined as

$$P(M|\theta) = \prod_{k=1}^{N} \frac{1}{\sigma\sqrt{2\,\pi}} exp\left\{ -\frac{1}{2\sigma^2}\left(f_k^{exp} - f_k^{model}\right)^2 \right\}, \tag{2}$$

where the subscript k is used to indicate corresponding experimental f_k^{exp} and computed frequencies f_k^{model} (where $f_k^{model} = \frac{\omega_k}{2\pi}$, with ω_k solution of the above equations for a given c_{ij}). The σ parameter quantifies the overall experimental variability that is not accounted for by the parameters of the model (*e.g.* sensitivity to sample positioning, mass loading effects). To find the true posterior distribution, we use a Python implementation, called *emcee,* of the affine-invariant ensemble sampler for Markov Chain Monte Carlo (MCMC) proposed by Goodman & Weare [18]. This method allows solving the inverse problem as a distribution of samples converging to the true underlying posterior probability. As is usual with MCMC methods, we carefully monitored convergence of the sampler and discarded burn-in samples.

Regarding the elastic model parameters, *i.e.* the way the c_{ij} are defined, we use three models described in the next sections. First, an isotropic model is used for the elastic description of the S620 samples. Second, two elastic anisotropic models are used for the 316 L samples: the effective orthotropic elastic model and the EBSD measurement-based model.

2.4.2. S620 sample inversion: Isotropic elastic model

The S620 samples were described by an isotropic elastic model, *i.e.* elasticity that is invariant with the rotation of the crystallographic frame of reference. Modelling a metallic polycrystalline sample as isotropic is usually justified when the sample is an aggregate of many small grains with random crystal orientations. Two elastic constants are necessary in this case. We used constants c_{11} and c_{44} for this, although other choices are possible. Using Voigt notation for the elastic constant matrix, this class of elasticity leads to the following c_{ij} tensor:

$$\mathbf{c}_{\mathrm{ij}}^{\mathrm{isotropic}} = \begin{bmatrix} \mathrm{c}_{11} & \mathrm{c}_{11}-2\mathrm{c}_{44} & \mathrm{c}_{11}-2\mathrm{c}_{44} & 0 & 0 & 0 \\ \mathrm{c}_{11}-2\mathrm{c}_{44} & \mathrm{c}_{11} & \mathrm{c}_{11}-2\mathrm{c}_{44} & 0 & 0 & 0 \\ \mathrm{c}_{11}-2\mathrm{c}_{44} & \mathrm{c}_{11}-2\mathrm{c}_{44} & \mathrm{c}_{11} & 0 & 0 & 0 \\ 0 & 0 & 0 & \mathrm{c}_{44} & 0 & 0 \\ 0 & 0 & 0 & 0 & \mathrm{c}_{44} & 0 \\ 0 & 0 & 0 & 0 & 0 & \mathrm{c}_{44} \end{bmatrix}. \tag{3}$$

2.4.3. 316 L sample inversion: effective orthotropic elastic model

When the sample exhibits crystallographic texture, *i.e.* when crystal orientations are not randomly distributed, elastic behaviour becomes more complex. To model the elasticity of the 316 L austenitic steel samples, we used an orthotropic model. This describes its elasticity using nine coefficients. The resulting c_{ij} matrix reads:

$$\mathbf{c}_{\mathrm{ij}}^{\mathrm{orthotropic}} = \begin{bmatrix} \mathrm{c}_{11} & \mathrm{c}_{12} & \mathrm{c}_{13} & 0 & 0 & 0 \\ \mathrm{c}_{12} & \mathrm{c}_{22} & \mathrm{c}_{23} & 0 & 0 & 0 \\ \mathrm{c}_{13} & \mathrm{c}_{23} & \mathrm{c}_{33} & 0 & 0 & 0 \\ 0 & 0 & 0 & \mathrm{c}_{44} & 0 & 0 \\ 0 & 0 & 0 & 0 & \mathrm{c}_{55} & 0 \\ 0 & 0 & 0 & 0 & 0 & \mathrm{c}_{66} \end{bmatrix}. \tag{4}$$

This choice of elastic tensor rests on the hypothesis that the elasticity can effectively be represented by a medium that possesses three mutually orthogonal planes of symmetry, such as is *e.g.* the case for a rolled metal sheet. A similar model has already been used as the effective elastic constants of a an additively manufactured nickel-based polycrystal in [10]. To justify this assumption, we have to consider how the effective elastic properties at the sample scale are related to the elastic properties at the crystallite level. One of the simplest ways to do this is to use the Voigt, Reuss and Hill (VRH) models of aggregate elasticity [10]. The Voigt model assumes constant strain in all crystallites, while the Reuss model assumes constant stress. These assumptions lead to aggregate elastic constants computed as volume weighted stiffness of grains (Voigt case) or volume weighted compliances of grains (Reuss case) [19]. The Hill averaged tensor is the average of the elastic tensor obtained by the two previous methods. Without going further, we can then say that the orthotropic model is the hypothetic elastic Hill average model corresponding to the metallic 316 L polycrystal. The resonant ultrasound model can then determine the best fitting elastic module within this class of models based on the measured resonant peaks.

A different model, that relies on the already described VRH models of elastic homogenization, is the texture-based model described in the next section.

2.4.4. EBSD texture-based elastic model using the Hill averaging scheme

As described above, the Voigt and Reuss models lead to volume-weighted averages of elastic constants. The elastic tensor within a grain can be modelled by single crystal elastic constants that are "rotated" within each grain, taking into account the geometrical transformation relating the crystal to the sample reference frame. This is usually written $C_{ij}^{rotated} = M{\cdot}c_{ij}^{SC}{\cdot}M^T$, where $C_{ij}^{rotated}$ is the single crystal elastic tensor in sample reference frame, c_{ij}^{SC} is the single crystal elastic tensor in crystal aligned reference frame and M the matrix representing the change of coordinate for the fourth order tensor in Voigt notation [20]. Using the Bunge Euler angles convention $\varphi_1, \Phi, \varphi_2$ and using the fact that austenite is cubic [21,23], we compute the Voigt and Reuss elastic constants and then take the Hill average $c_{ij}^{Hill} = \frac{1}{2}c_{ij}^{Voigt} + \frac{1}{2}c_{ij}^{Reuss}$ based on the single crystal values for the whole material, as in [22,24,25]. We use the texture data measured by EBSD as input for the Bunge Euler angles at each pixel and average over each pixel of the region of interest, to be representative of the volume. These elastic constants are used to solve the RUS inverse problem and fit the single crystal elastic constants to the recorded data. This model is depicted schematically in Fig. 4.

Due to the grid-like nature of the EBSD image, the Voigt elastic tensor

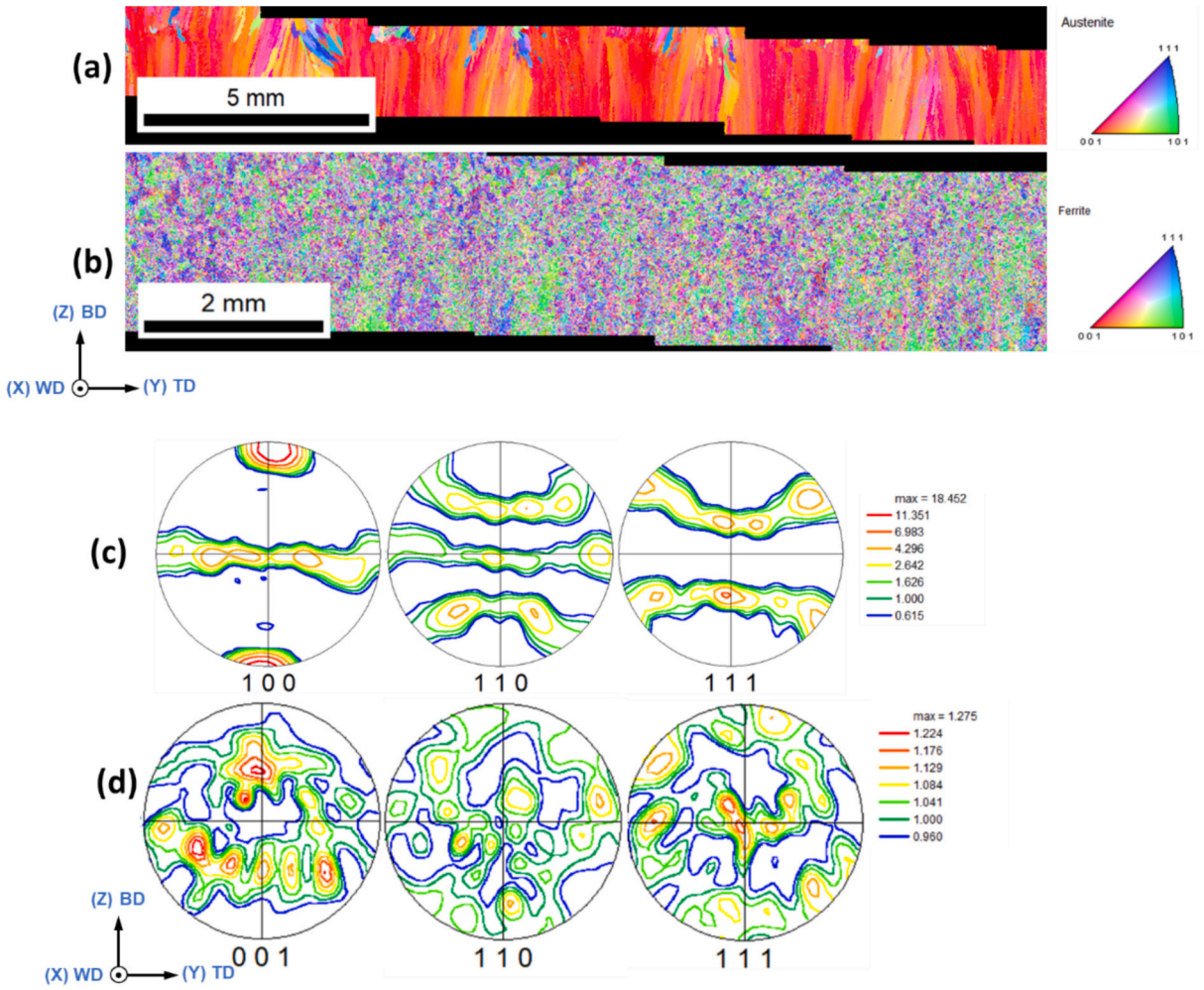

Fig. 5. (a) and (b): BD-IPF maps of 316 L and S620 steels respectively, (c) and (d) The pole figures of 316 L and S620 steels, respectively.

becomes an average over the N valid pixels in the image: $c_{ij}^{Voigt} = \frac{1}{N}\sum_{i=1}^{N} M_i \cdot c_{ij}^{SC} \cdot M_i^T$, c_{ij}^{SC} is the single crystal elastic tensor and M the matrix representing the change of coordinate for the fourth order tensor in Voigt notation [20]. In order to avoid repeating this computation for varying single-crystal parameters c_{11}, c_{12}, c_{44}, we linearly decompose the cubic single-crystal matrix in the form $c_{ij}^{SC} = c_{11}K_{c_{11}} + c_{12}K_{c_{12}} + c_{44}K_{c_{44}}$

In the above formula, the parenthesized expressions can be computed once and then reused for fast evaluation of the Voigt elastic tensor when the single crystal parameters are varied.

A similar expression can be derived in terms of stiffnesses s_{11}, s_{12}, s_{44} for the Reuss average $c_{ij}^{Reuss} = \left[\frac{1}{N}\sum_{i=1}^{N}\left(M_i \cdot c_{ij}^{SC} \cdot M_i^T\right)^{-1}\right]^{-1}$:

$$c_{ij}^{Reuss} = s_{11}\left(\frac{1}{N}\sum_{i=1}^{N}\left(M_i^T\right)^{-1}\cdot K_{c_{11}}\cdot M_i^{-1}\right) + s_{12}\left(\frac{1}{N}\sum_{i=1}^{N}\left(M_i^T\right)^{-1}\cdot K_{c_{12}}\cdot M_i^{-1}\right) + s_{44}\left(\frac{1}{N}\sum_{i=1}^{N}\left(M_i^T\right)^{-1}\cdot K_{c_{44}}\cdot M_i^{-1}\right). \quad (6)$$

where $K_{c_{11}}, K_{c_{12}}, K_{c_{44}}$ are 6×6 Voigt matrices containing only ones and zeros. Factoring out the scalar constants leads to the following expression:

where $s_{11} = \frac{c_{11}+c_{12}}{c_{11}^2+c_{11}c_{12}-2c_{12}^2}$, $s_{12} = -\frac{c_{12}}{c_{11}^2+c_{11}c_{12}-2c_{12}^2}$, $s_{44} = \frac{1}{c_{44}}$. As with the formula for the Voigt average, the expressions in parentheses can be computed once and reused for multiple evaluations while varying the input values of c_{11}, c_{12}, c_{44}, which are unknown and hence can be set to

$$c_{ij}^{Voigt} = c_{11}\left(\frac{1}{N}\sum_{i=1}^{N} M_i\cdot K_{c_{11}}\cdot M_i^T\right) + c_{12}\left(\frac{1}{N}\sum_{i=1}^{N} M_i\cdot K_{c_{12}}\cdot M_i^T\right) + c_{44}\left(\frac{1}{N}\sum_{i=1}^{N} M_i\cdot K_{c_{44}}\cdot M_i^T\right). \quad (5)$$

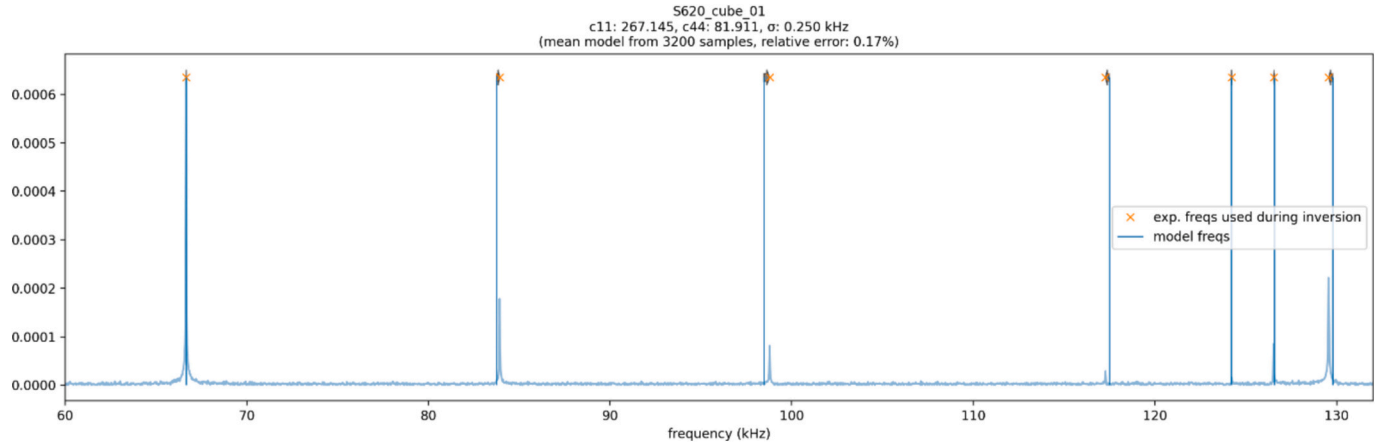

Fig. 6. RUS inversion result for S620 sample 1. The measured spectrum is shown along with extracted peaks as crosses, and the fitted model shown as vertical bars.

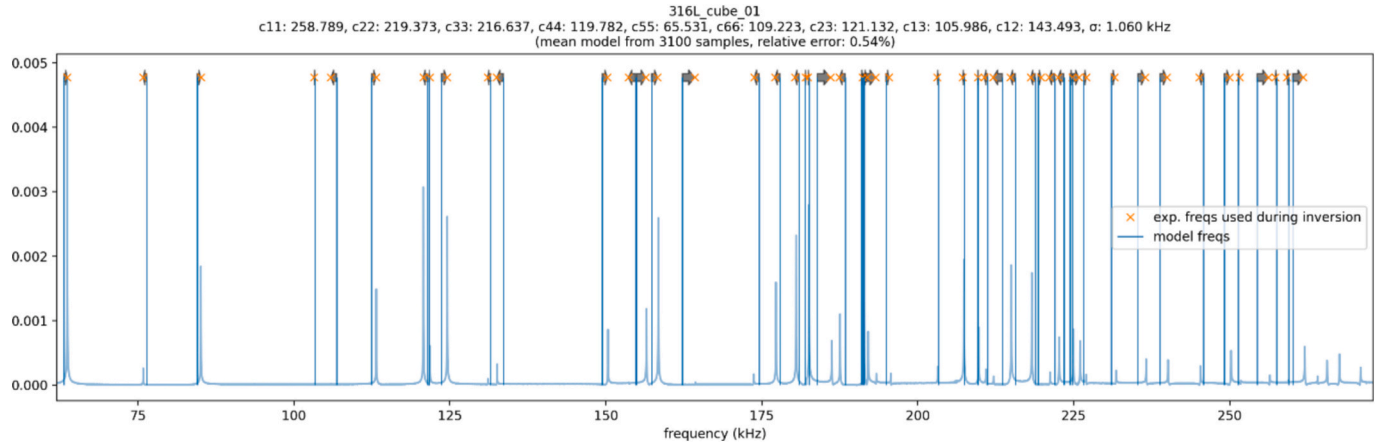

Fig. 7. Effective orthotropic RUS inversion result for 316 L sample 1. The measured spectrum is shown along with extracted peaks as crosses, and the fitted model shown as vertical bars.

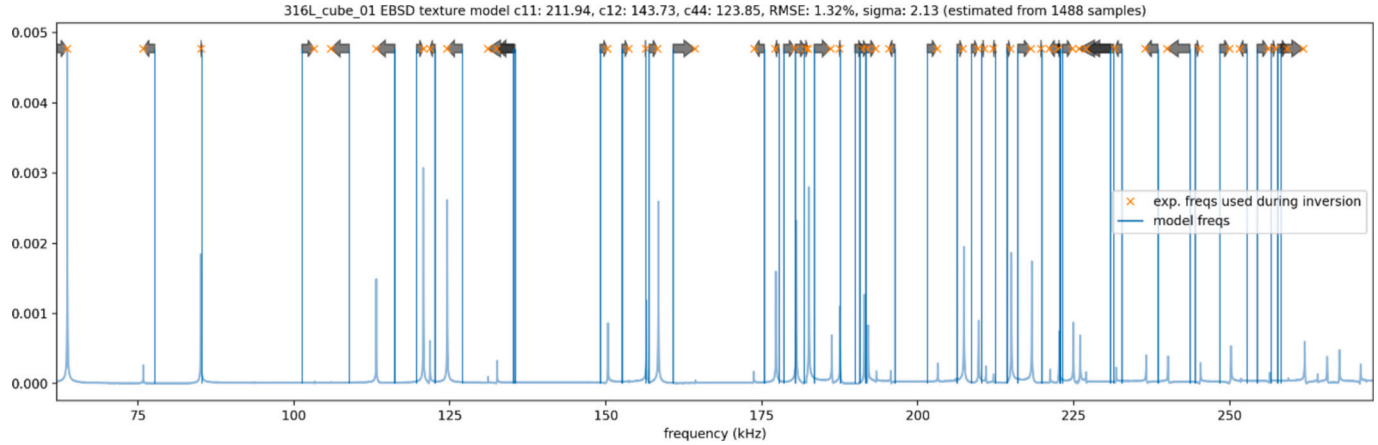

Fig. 8. EBSD texture-based elastic model inversion result for 316 L sample 1. The measured spectrum is shown along with extracted peaks as crosses, and the fitted model shown as vertical bars.

"optimal" values inferred from the resonance frequency measurement.

The obtained Hill elastic constants c_{ij}^{Hill} are then used as inputs within the Bayesian inversion algorithm described in subsection 2.4.1.

The next section discusses the results obtained by the measurement techniques described in this section.

3. Results

3.1. Texture and physical analysis

Figure 5 displays the EBSD results, including the orientation maps, the pole figures and the inverse pole figures (using the build direction,

```
[[258.79, 143.49, 105.99,   0.  ,   0.  ,   0.  ],
 [143.49, 219.37, 121.13,   0.  ,   0.  ,   0.  ],
 [105.99, 121.13, 216.64,   0.  ,   0.  ,   0.  ],
 [  0.  ,   0.  ,   0.  , 119.78,   0.  ,   0.  ],
 [  0.  ,   0.  ,   0.  ,   0.  ,  65.53,   0.  ],
 [  0.  ,   0.  ,   0.  ,   0.  ,   0.  , 109.22]]
```

a)

```
[[255.44 136.98 107.12   3.69   0.49   7.62]
 [136.98 222.98 139.58 -11.38  -1.57  -8.97]
 [107.12 139.58 252.84   7.69   1.08   1.35]
 [  3.69 -11.38   7.69 112.85   2.61  -1.88]
 [  0.49  -1.57   1.08   2.61  62.85   4.66]
 [  7.62  -8.97   1.35  -1.88   4.66 106.91]]
```

b)

Fig. 9. Comparison of elastic constants for 316 L sample 1 obtained by effective model (a) and EBSD texture based model (b).

Table 3
Inversion results for S620 samples obtained using the isotropic elastic RUS model.

Sample	c_{11} (GPa)	c_{44}(GPa)	σ (kHz)	RMS (%)
S620 sample 1	267.15 ± 4.00	81.91 ± 0.25	0.25 ± 0.10	0.17
S620 sample 2	266.39 ± 5.70	81.92 ± 0.44	0.34 ± 0.20	0.19

BD, as reference direction). This sample shows an austenitic microstructure consisting of grains that are mostly elongated in the build direction, as shown on Fig. 5a. The XRD measurement also confirmed the formation of a single austenitic structure during WAAM processing of 316 L stainless steel (see Fig. 2). The red colour predominance in the IPF map indicates that most austenite grains have a ⟨001⟩ direction aligned parallel to the building direction. The texture results of 316 L steel are also presented as pole figs. (PF) in Fig. 5c. The maximum intensity of ~18.4 MRD (multiples of a random density) in the PFs indicates the formation of a highly textured microstructure during 3D printing. Inspecting the (001) PF it shows that the ⟨001⟩ II BD fibre texture is the main texture component of the 316 L steel. Other studies have also reported the formation of a highly textured microstructure during additive manufacturing of 316 L steel [26,27].

Figure 5b shows the IPF map of S620 steel consisting of a microstructure of equiaxed grains. The deposited S620 steel exhibited a ferritic microstructure with a body-centred cubic (BCC) crystallographic structure. The PFs of steel S620, shown in Fig. 5d, reveal a maximum intensity of ~1.2MRD, indicating that the deposited S620 steel has a near-randomly textured microstructure. The solid-state phase transformations from austenite to ferrite can be considered the main factor responsible for the weak texture of S620 steel.

3.2. Elastic constants obtained by RUS

3.2.1. S620 isotropic elastic model

The results obtained using the isotropic model fit on S620 samples are shown in Table 3. The obtained RMS error, typically used in evaluating a RUS fit, is 0.2 %, well below the 0.8 % indicating a good fit [28], even though only seven peaks were used. This is further confirmed by the visual match between the recorded spectrum and the model for S620 sample 1, shown in Fig. 6. The Bayesian inverse model also provides error bars for the elastic constants, based on the noise model fit using the σ parameter. In this case, the errors σ and *RMS* are of a magnitude comparable to those found in the isotropic inversion in [14].

3.2.2. Effective orthotropic model applied to 316 L samples

The results obtained by applying the effective orthotropic model to the 316 L samples are shown in Table 4, along with the error estimates from the Bayesian model. The first fifty frequencies picked from the resonance spectra were used in these inversions. The obtained RMS error is below 0.8 % and no resonance frequencies have been missed, again suggesting this is a good fit [28], although the error figures are larger than in the previous S620 case.

As seen in Table 4, the 316 L samples exhibit a strong elastic anisotropy. While axes 1 and 3 have similar effective elastic constants, axis 2 stands out as having a significantly lower shear constant c_{55}. With our modelling choices, axis 2 is parallel to the build direction of the 316 L samples. Fig. 7 shows the comparison between the measured spectrum and the model peaks predicted by the best-fit parameters for 316 L sample 1.

3.2.3. EBSD texture-based elastic model

The EBSD texture-based model described in the previous sections leads to two sets of results. The Bayesian inversion infers the best single crystal constants from the resonance data, shown in Table 5. The first fifty frequencies picked from the resonance spectra of 316 L sample 1 were used in this inversion. In a subsequent step, the same constants of the elastic tensor already shown in Table 4 are also computed and shown in Table 6. Fig. 8 shows the obtained model along with the measured resonance data.

4. Discussion

This study dealt with the characterization of elastic and crystallographic properties of four samples, cut from walls that were manufactured by the WAAM technique. Two different wires were used, one composed of a low-alloy construction steel (S620), and the other one composed of an austenitic stainless steel (316 L). Resonant ultrasound spectroscopy was used as the primary analysis tool to probe the elastic behaviour of these samples, since it is particularly sensitive to elastic anisotropy because it measures all elastic constants simultaneously [29].

Table 5
Texture based model: single crystal elastic constants computed using Bayesian inversion and model error estimates σ and RMS.

Sample	c_{11} (GPa)	c_{12} (GPa)	c_{44}(GPa)	σ (kHz)	RMS (%)
31 6 L sample 1	211.94 ± 6.37	143.73 ± 6.68	123.85 ± 2.11	2.13 ± 0.22	1.32

Table 4
Inversion results for 316 L samples obtained using the effective orthotropic RUS model. The value indicated as ± is the standard deviation (*i.e.* the 16–84 % quartile).

Sample	c_{11}(GPa)	c_{22}(GPa)	c_{33}(GPa)	c_{44}(GPa)	c_{55}(GPa)	c_{66}(GPa)	c_{23}(GPa)	c_{13}(GPa)	c_{12}(GPa)	σ (kHz)	RMS (%)
316 L sample 1	258.48 ± 10.24	219.78 ± 6.61	216.81 ± 7.56	119.64 ± 3.37	65.50 ± 0.88	109.19 ± 1.56	120.97 ± 7.45	106.13 ± 6.53	143.15 ± 8.78	1.07 ± 0.15	0.53
316 L sample 2	249.70 ± 9.71	221.44 ± 9.53	228.97 ± 10.64	115.44 ± 3.10	66.51 ± 1.02	112.49 ± 1.88	130.06 ± 10.06	110.15 ± 9.29	141.61 ± 10.20	1.24 ± 0.11	0.72

Table 6
Texture-based model: elastic constants computed from the single crystal fit with associated uncertainties.

Sample	c_{11}(GPa)	c_{22}(GPa)	c_{33}(GPa)	c_{44}(GPa)	c_{55}(GPa)	c_{66}(GPa)	c_{23}(GPa)	c_{13}(GPa)	c_{12}(GPa)
316 L sample 1	256.14 ± 6.68	223.23 ± 6.93	253.51 ± 6.71	113.00 ± 1.69	62.85 ± 0.21	106.99 ± 1.40	140.38 ± 6.62	107.54 ± 7.15	137.75 ± 6.66

EBSD imaging was used to confirm the RUS conclusions.

The S620 samples resonant spectrums were found to be a good fit with an isotropic elastic model. Additional EBSD data gave a good explanation for this result, as the microstructure consisted of small grains with a nearly random crystallographic texture. This explained the observed elastic isotropy [30].

However, the isotropic model could not be applied satisfactorily to the 316 L samples (*i.e.* the resonance frequencies could not be fitted with error below 0.8 % using this two independant elastic constants model). Therefore, we have used two different models with a larger number of elastic constants to fit the 316 L resonance data. The *effective* model assumes orthotropic elastic behaviour of the sample, described by nine independant elastic constants. The EBSD texture based model assumes that the orientation statistics observed by EBSD can be used within the Hill homogenization procedure, in combination with a cubic description of the 316 L single crystal elasticity (three independent elastic constants). These two models have been used to infer elastic constants from the resonant spectra that were measured on 316 L sample 1. As shown in the results section, both models give different elastic constants of the same order of magnitude. In particular, both models show that the c_{55} modulus, which is the shear constant related to axis 2, corresponding to the grain elongation axis and build direction, is softer than the c_{44} and c_{66} (respectively the transverse and weld direction). Fig. 9 shows the elastic tensors corresponding to one of the polycrystalline 316 L samples using the two models. There is a satisfactory agreement between the two methods for almost all elastic constants, differences being usually less than 10 GPa and often less than 5 GPa.

However, there were remaining differences between the models and the question arose whether or not one model is better than the other. Fig. 9 particularly shows that the effective model has many elastic constants that are zero where the texture-based model has small values, almost all below 10 GPa (if these constants are set to 0 GPa, the average error incurred on the first 50 frequencies is just 0.7 %). The zero values are a consequence of the hypothesis that the effective microstructure is orthotropic with orthotropic axes being aligned with the sample directions, but is difficult to justify theoretically. Other authors have used similar hypotheses for Inconel 625, including further free parameters in the form of Euler angles that rotate the effective microstructure reference frame [10].

The EBSD-measured texture model should be a better model in the sense that it takes into account the true effects of crystallographic anisotropy but as results have shown, it performs worse in terms of σ and RMS error. One reason for this could be that the "true" material texture is less accurately represented by the texture-based model than by the effective model. This could be either due to the cubic elasticity hypothesis of the 316 L single crystal, but this seems unlikely in the light of previous work [31]. Another possibility would be that the measured texture is a biased sampling of the average texture of the sample, for example due to measuring only a few dozens of grains on the surface out of the millions in the sample bulk. This situation could be similar to the one encountered by Rossin et al. [12] when comparing EBSD-measured texture to neutron diffraction data and finding partial disagreement. Reasoning purely in terms of model parameters, another explanation could be that the texture model has only three free parameters, the cubic single crystal constants, while the effective model has nine, allowing greater flexibility and thus lower mismatches.

The present work also allowed the characterization of the single crystal constants from the bulk data in a similar framework than the one introduced by Rossin et al. [12]. Our results are in good agreement with the values from Ledbetter [31], who mentions values of 207, 133 and 117 GPa for c_{11}, c_{12}, c_{44}, while we find 211.94, 143.73 and 123.85. Of course, our approach does not give significant insights into this particular material, but could be applied to novel materials that exhibit significant anisotropy and cannot be easily grown as single crystals, as mentioned in [12].

The elastic constants found using RUS reflect the underlying crystallographic texture of the samples used in the study. Since the 316 L sample is highly anisotropic, we could actually go even further and try transforming the elastic constants to a texture representation. This could be done using either the 2nd order Hashin-Shtrikman tensorial ODF representation such as done in Rossin et al. [11] or the spherical convolution model of wave velocities proposed by Lan et al. [32].

5. Conclusions

In this article, we have investigated rectangular samples machined from walls of 316 L and S620 steel wires fabricated with the WAAM process. Several analysis techniques were applied to the samples to reveal their elastic and structural characteristics. Resonant ultrasound spectroscopy was used to measure the vibrational spectrum of samples and fit elastic constants to it, EBSD to characterize its texture and XRD its crystal structure. The RUS method led us to conclude the S620 construction steel exhibits isotropic elastic behaviour, which was confirmed by the random texture as observed by EBSD. The elastic behaviour of the 316 L polycrystals, however, was found to be strongly anisotropic. We used two RUS inverse models to analyse the elastic anisotropy: first, an effective model supposing orthotropic elastic symmetry, and second, a texture-based model applying the Hill average scheme to compute elastic constants based on a cubic single crystal elasticity hypothesis. The RUS inverse model based on EBSD texture fit was of less quality than the one of the effective orthotropic model, but provided a physical understanding of the loss of elastic stiffness along the build axis direction. EBSD confirmed that the elastic anisotropy was linked to the strong texture due to <001> directions aligned parallel to the building direction. This particular conclusion has already been well documented for austenitic welds with fibre-like texture [31], however we show that it also applies to this WAAM fabricated sample. This study also suggests that RUS is well suited for characterizing anisotropy in additively manufactured samples.

CRediT authorship contribution statement

Florian Le Bourdais: Writing – original draft, Visualization, Software, Methodology, Investigation, Formal analysis, Data curation, Conceptualization. **Mahdi Mahmoudiniya:** Writing – review & editing, Methodology, Investigation, Conceptualization. **Audrey Gardahaut:** Writing – review & editing, Project administration, Investigation, Funding acquisition, Data curation, Conceptualization. **Leo A.I. Kestens:** Writing – review & editing, Validation, Supervision, Funding acquisition, Formal analysis, Conceptualization.

Declaration of competing interest

The authors declare that they have no known competing financial interests or personal relationships that could have appeared to influence the work reported in this paper.

Data availability

The data that has been used is confidential.

Acknowledgments

This project has received funding from the European Union's Horizon 2020 research and innovation programme under grant agreement no 862017 (Grade2XL).

We thank Anne-Sophie Thorr (Naval Group) for providing the coupons part of the study within the Grade2XL project as well as helpful build information. We thank José Luis Galán Argumedo (TU Delft) for constructive discussions regarding this manuscript.

References

[1] F. Honarvar, A. Varvani-Farahani, A review of ultrasonic testing applications in additive manufacturing: defect evaluation, material characterization, and process control, Ultrasonics 108 (2020) 106227, https://doi.org/10.1016/j.ultras.2020.106227.

[2] A. Migliori, et al., Resonant ultrasound spectroscopic techniques for measurement of the elastic moduli of solids, Phys. B Condens. Matter 183 (1–2) (1993) 1–24, https://doi.org/10.1016/0921-4526(93)90048-B.

[3] B.J. Zadler, J.H. Le Rousseau, J.A. Scales, M.L. Smith, Resonant ultrasound spectroscopy: theory and application, Geophys. J. Int. 156 (1) (2004) 154–169.

[4] K. Flynn, M. Radovic, Evaluation of defects in materials using resonant ultrasound spectroscopy, J. Mater. Sci. 46 (8) (2011) 2548–2556, https://doi.org/10.1007/s10853-010-5107-y.

[5] S. McGuigan, A.P. Arguelles, A.-F. Obaton, A.M. Donmez, J. Riviere, P. Shokouhi, Resonant ultrasound spectroscopy for quality control of geometrically complex additively manufactured components, Addit. Manuf. 39 (2021) 101808, https://doi.org/10.1016/j.addma.2020.101808.

[6] A.-F. Obaton, G. Weaver, L.F. Fayard, F. Montagner, O. Burnet, A. Van den Bossche, Classification of metal PBF-LB parts manufactured with different process parameters using resonant ultrasound spectroscopy, Weld World 67 (4) (2023) 1091–1103, https://doi.org/10.1007/s40194-022-01419-w.

[7] E. Bozek, C.L. Williams, J. Rivière, P. Shokouhi, Nonlinear/linear resonance ultrasound spectroscopy (N/RUS) of additively manufactured 316L stainless steel samples using in-contact and non-contact excitation, NDT & E Internat. 140 (2023) 102948, https://doi.org/10.1016/j.ndteint.2023.102948.

[8] P. Manogharan, J. Rivière, P. Shokouhi, Toward in-situ characterization of additively manufactured parts using nonlinear resonance ultrasonic spectroscopy, Res. Nondestruct. Eval. 33 (4–5) (2022) 243–266, https://doi.org/10.1080/09349847.2022.2103219.

[9] F. Le Bourdais, et al., On the potential of resonant ultrasound spectroscopy applied to the non-destructive characterization of the density of (LPBF) additively manufactured materials, Addit. Manuf. 58 (2022) 103037, https://doi.org/10.1016/j.addma.2022.103037.

[10] J. Rossin, et al., Assessment of grain structure evolution with resonant ultrasound spectroscopy in additively manufactured nickel alloys, Mater. Charact. 167 (2020) 110501, https://doi.org/10.1016/j.matchar.2020.110501.

[11] J. Rossin, et al., Bayesian inference of elastic constants and texture coefficients in additively manufactured cobalt-nickel superalloys using resonant ultrasound spectroscopy, Acta Mater. 220 (2021) 117287, https://doi.org/10.1016/j.actamat.2021.117287.

[12] J. Rossin, et al., Single crystal elastic constants of additively manufactured components determined by resonant ultrasound spectroscopy, Mater. Charact. 192 (2022) 112244, https://doi.org/10.1016/j.matchar.2022.112244.

[13] J. Rossin, Additively Manufactured Alloy Characterization with Resonant Ultrasound Spectroscopy, University of California Santa Barbara, 2022.

[14] B. Bales, L. Petzold, B.R. Goodlet, W.C. Lenthe, T.M. Pollock, Bayesian inference of elastic properties with resonant ultrasound spectroscopy, J. Acoust. Soc. Am. 143 (1) (2018) 71–83, https://doi.org/10.1121/1.5017840.

[15] Jrossin, Texture-RUS, Python, 2021. Accessed: Sep. 17, 2021. [Online]. Available: https://github.com/jrossin/texture-RUS.

[16] M. Newville, T. Stensitzki, D.B. Allen, A. Ingargiola, LMFIT: Non-Linear Least-Square Minimization and Curve-Fitting for Python, Zenodo, 2014, https://doi.org/10.5281/zenodo.11813.

[17] W.M. Visscher, A. Migliori, T.M. Bell, R.A. Reinert, On the normal modes of free vibration of inhomogeneous and anisotropic elastic objects, J. Acoust. Soc. Am. 90 (4) (1991) 2154–2162, https://doi.org/10.1121/1.401643.

[18] D. Foreman-Mackey, D.W. Hogg, D. Lang, J. Goodman, Emcee: the MCMC hammer, Publ. Astron. Soc. Pac. 125 (925) (2013) 306–312, https://doi.org/10.1086/670067.

[19] R. Hill, Elastic properties of reinforced solids: some theoretical principles, J. Mech. Phys. Solids 11 (5) (1963) 357–372, https://doi.org/10.1016/0022-5096(63)90036-X.

[20] W.L. Bond, The mathematics of the physical properties of crystals, Bell Syst. Tech. J. 22 (1) (1943) 1–72, https://doi.org/10.1002/j.1538-7305.1943.tb01304.x.

[21] B. Lan, M. Lowe, F.P.E. Dunne, Experimental and computational studies of ultrasound wave propagation in hexagonal close-packed polycrystals for texture detection, Acta Mater. 63 (2014) 107–122, https://doi.org/10.1016/j.actamat.2013.10.012.

[22] C. Kim, H. Yin, A. Shmatok, B.C. Prorok, X. Lou, K.H. Matlack, Ultrasonic nondestructive evaluation of laser powder bed fusion 316L stainless steel, Addit. Manuf. 38 (2021) 101800, https://doi.org/10.1016/j.addma.2020.101800.

[23] A. Teklu, H. Ledbetter, S. Kim, L.A. Boatner, M. McGuire, V. Keppens, Single-crystal elastic constants of Fe-15Ni-15Cr alloy, Metall. Mater. Trans. A 35 (10) (2004) 3149–3154, https://doi.org/10.1007/s11661-004-0059-y.

[24] D.H. Hurley, S.J. Reese, F. Farzbod, Application of laser-based resonant ultrasound spectroscopy to study texture in copper, J. Appl. Phys. 111 (5) (2012) 053527, https://doi.org/10.1063/1.3692386.

[25] M.I. Latypov, et al., Computational homogenization for multiscale forward modeling of resonant ultrasound spectroscopy of heterogeneous materials, Mater. Charact. 158 (2019) 109945, https://doi.org/10.1016/j.matchar.2019.109945.

[26] T.F.W. van Nuland, L. Palmeira Belotti, J.P.M. Hoefnagels, J.A.W. van Dommelen, M.G.D. Geers, Microstructural modeling and measurements of anisotropic plasticity in large scale additively manufactured 316L stainless steel, Eur. J. Mechan. - A/Solids 96 (2022) 104710, https://doi.org/10.1016/j.euromechsol.2022.104710.

[27] L. Palmeira Belotti, J.A.W. van Dommelen, M.G.D. Geers, C. Goulas, W. Ya, J.P. M. Hoefnagels, Microstructural characterisation of thick-walled wire arc additively manufactured stainless steel, J. Mater. Process. Technol. 299 (2022) 117373, https://doi.org/10.1016/j.jmatprotec.2021.117373.

[28] J. Torres, A. Flores-Betancourt, R.P. Hermann, *RUScal* : software for the analysis of resonant ultrasound spectroscopy measurements, J. Acoust. Soc. Am. 151 (5) (2022) 3547–3563, https://doi.org/10.1121/10.0011397.

[29] R.G. Leisure, F.A. Willis, Resonant ultrasound spectroscopy, 1997, p. 30.

[30] M. Hirao, K. Aoki, H. Fukuoka, Texture of polycrystalline metals characterized by ultrasonic velocity measurements, J. Acoust. Soc. Am. 81 (5) (1987) 1434–1440, https://doi.org/10.1121/1.394495.

[31] H.M. Ledbetter, Monocrystal elastic constants in the ultrasonic study of welds, Ultrasonics 23 (1) (1985) 9–13, https://doi.org/10.1016/0041-624X(85)90005-8.

[32] B. Lan, M.A. Carpenter, W. Gan, M. Hofmann, F.P.E. Dunne, M.J.S. Lowe, Rapid measurement of volumetric texture using resonant ultrasound spectroscopy, Scr. Mater. 157 (2018) 44–48, https://doi.org/10.1016/j.scriptamat.2018.07.029.